RSC Advances

PAPER

View Article Online
View Journal | View Issue

Check for updates

Cite this: *RSC Adv.*, 2022, **12**, 27125

Particle size effect on millimeter-wave absorption, rotation, and ellipticity of gallium-substituted epsilon iron oxide†

Shoma Shimizu, Asuka Namai * and Shin-ichi Ohkoshi *

Received 23rd May 2022
Accepted 19th September 2022

DOI: 10.1039/d2ra03237f

rsc.li/rsc-advances

Various applications employ millimeter waves. For example, the carrier frequencies of vehicle radar in advanced driver assistance systems are 76–81 GHz millimeter waves. Here, we investigate the particle size effect on millimeter-wave absorption of gallium-substituted epsilon iron oxide ε-$Ga_xFe_{2-x}O_3$ with $x = 0.44 \pm 0.01$. Samples were composed of nanoparticles with sizes of 16.9(1) nm, 28.8(2) nm, and 41.4(1) nm. Millimeter wave absorption, Faraday rotation, and Faraday ellipticity were measured by terahertz time-domain spectroscopy. This series exhibits millimeter-wave absorption at 78.7, 78.2, and 77.7 GHz without an external magnetic field. The millimeter-wave absorption increases from 4.6 dB to 9.4 dB as the particle size increases. In the magnetized sample, the Faraday rotation angle increases from 9.1° to 18.4°, while the Faraday ellipticity increases from 0.27 to 0.52. The particle size effect can be explained by the change in the ratio of the surface and core of the nanoparticles. The present study should contribute to the realization of high-performance millimeter-wave absorbers.

Open Access Article. Published on 23 September 2022. Downloaded on 2/28/2025 12:12:53 PM.
This article is licensed under a Creative Commons Attribution-NonCommercial 3.0 Unported Licence.

Introduction

Advanced driver assistance systems (ADAS) for automobiles are becoming ubiquitous.[1,2] Millimeter-wave car radars (76.5 GHz, 79 GHz, and 81 GHz) are equipped in ADAS for forward monitoring because they are less susceptible to weather conditions such as rain and fog.[3,4] Additionally, the demand for technologies to suppress noise and electromagnetic interference is increasing.[5,6] Consequently, the development of millimeter-wave absorbers and circulators is an important issue. Magnetic materials can absorb electromagnetic waves, which are due to magnetic loss.[7–15] However, the absorption frequencies of magnetic materials such as ferrite and metal are generally low compared to the carrier frequency of millimeter-wave car radar.[16,17] Epsilon iron oxide ε-Fe_2O_3 nanomagnets have attracted much attention. They exhibit large magnetic anisotropy and high-frequency millimeter-wave absorption.[18–45] Additionally, metal-substituted epsilon iron oxide, ε-$M_xFe_{2-x}O_3$,[46–70] exhibits millimeter-wave absorption in the range of 35–222 GHz, in which the resonance frequency is controlled by a kind of substitution metal and substitution ratio. Recently, the resonance frequency shift due to change on the particle size of ε-Fe_2O_3 nanomagnets has been also reported.[45]

Gallium-substituted epsilon iron oxide ε-$Ga_xFe_{2-x}O_3$ is suitable for the resonance of the millimeter-wave car radar frequency and should serve as a millimeter-wave absorber.[52] To enhance the millimeter-wave absorption, we investigate the effect of particle size on the millimeter-wave absorption properties of ε-$Ga_xFe_{2-x}O_3$ nanoparticles. In the present work, ε-$Ga_xFe_{2-x}O_3$ with different nanoparticle sizes are prepared by changing the sintering temperature in the range of 1050–1150 °C. Then the magnetic properties and millimeter-wave absorption are measured. In addition, Faraday rotation and Faraday ellipticity are also measured from the viewpoint of application for millimeter wave devices such as isolators and circulators. Finally, the particle size effect is discussed.

Results and discussion

Materials, crystal structure, and morphology

The samples were prepared by the sol–gel method according to the literature.[52] Iron nitrate and gallium nitrate were dissolved in water with a ratio of Ga : Fe = 0.46 : 1.54, and ammonia and tetraethyl orthosilicate were added successively to obtain precursors. The precursors were sintered in air for 4 hours. To etch the silica matrix, the sintered samples were heated with a sodium hydroxide aqueous solution at 60 °C for 1 day. Three samples were prepared at different sintering temperatures: 1050 °C (**1**), 1100 °C (**2**), and 1150 °C (**3**).

Elemental analyses with inductively coupled plasma mass spectroscopy indicates that the formulas of the obtained samples are ε-$Ga_xFe_{2-x}O_3$, where $x = 0.43(1)$ for **1**, 0.45(1) for **2**, and 0.45(2) for **3**. The powder X-ray diffraction (PXRD) patterns

Department of Chemistry, School of Science, The University of Tokyo, 7-3-1 Hongo, Bunkyo-ku, Tokyo 113-0033, Japan. E-mail: asuka@chem.s.u-tokyo.ac.jp; ohkoshi@chem.s.u-tokyo.ac.jp

† Electronic supplementary information (ESI) available. See https://doi.org/10.1039/d2ra03237f

© 2022 The Author(s). Published by the Royal Society of Chemistry

Open Access Article. Published on 23 September 2022. Downloaded on 2/28/2025 12:12:53 PM.
This article is licensed under a Creative Commons Attribution-NonCommercial 3.0 Unported Licence.

show that all samples have an isomorphic structure of ε-Fe_2O_3 (orthorhombic structure, space group of $Pna2_1$) (Fig. S1 and Table S1†). The crystal structure has four non-equivalent metal sites (A–D sites) (Fig. 1a). The Ga ion tends to substitute the D site. The crystalline size evaluated from the PXRD patterns using the FP method (d_{FP}) increases as the sintering temperature increases: 16.9(1) nm for **1**, 28.8(2) nm for **2**, and 41.4(1) nm for **3**. TEM images confirm that the obtained samples are composed of nanoparticles (Fig. S2†). The particle size evaluated from the TEM images also becomes larger as the sintering temperature increases: 15 ± 6 nm (**1**), 23 ± 11 nm (**2**), and 33 ± 18 nm (**3**) (Fig. 1b).

Magnetic properties

The magnetic hysteresis was measured at 300 K using a superconducting quantum interference device (SQUID) magnetometer. The coercive fields are 4.1 (**1**), 7.1 (**2**), and 7.5 kOe (**3**) (Fig. 1c). The magnetization values at 5 tesla are 21.5 (**1**), 25.3 (**2**), and 26.7 emu g^{-1} (**3**). The magnetism of ε-$Ga_xFe_{2-x}O_3$ is classified as a ferrimagnet, where the sublattice magnetizations at the B and C sites are positive, while the sublattice magnetizations at the A and D sites are negative.[71–76] The D site has a smaller sublattice magnetization than those at the other sites, resulting in the appearance of ferrimagnetism.

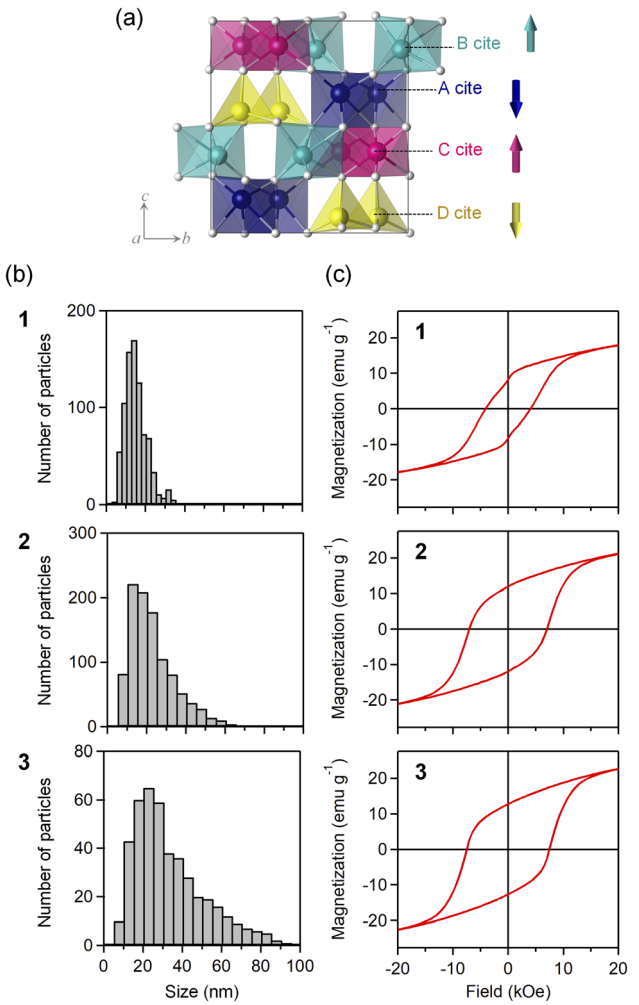

Fig. 1 (a) Crystal structure of ε-$Ga_xFe_{2-x}O_3$. Arrows indicate the sublattice magnetization directions of ε-$Ga_xFe_{2-x}O_3$. (b) The distribution of particle size measured from the TEM images. (c) Magnetic hysteresis loops measured at 300 K.

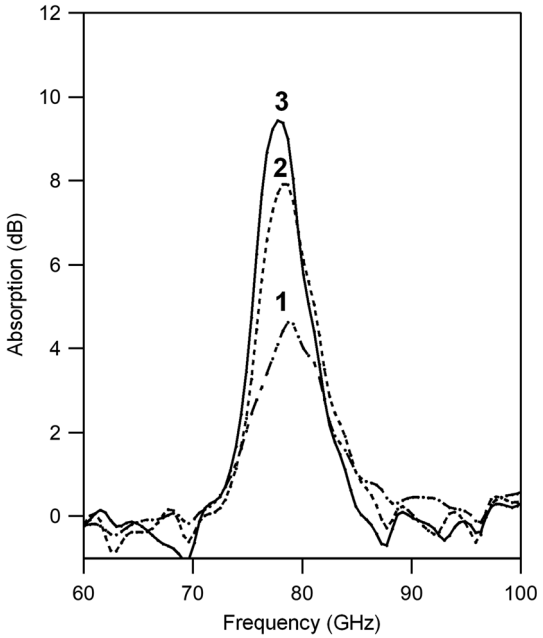

Fig. 2 Millimeter-wave absorption spectra for **1** (dashed line), **2** (dotted line), and **3** (solid line).

Millimeter-wave absorption

The millimeter-wave absorption was measured by using a terahertz time-domain spectroscopy (THz-TDS) system. To measure millimeter-wave absorption, a THz pulse was irradiated to the pellet-formed sample and a transmitted THz pulse and reflected pulse were obtained (Fig. S3†). Powder-formed samples were compressed into pellets (diameter: 13 mm ϕ) with a thickness of 1.02 (**1**), 0.98 (**2**), and 1.00 mm (**3**). The filling ratios were 56.8 (**1**), 59.5 (**2**), and 59.2 vol% (**3**). Fig. 2 shows the millimeter-wave absorption spectra. All samples have absorption peaks due to the natural resonance at 78.7 (**1**), 78.2 (**2**), 77.7 GHz (**3**). The millimeter-wave absorption increases with increasing the particle size: 4.6 (**1**), 7.9 (**2**), and 9.4 dB (**3**). The absorption peak area also increased as 38 (**1**), 52 (**2**), and 56 dB GHz (**3**).

Faraday rotation and ellipticity in the millimeter-wave region

To measure the Faraday rotation and ellipticity in the millimeter-wave region, wire grid polarizers were introduced in the THz-TDS system.[47,53,57] Polarizers were placed after the emitter and before the detector to precisely define the polarization of the THz pulse as horizontal. The vertical and horizontal components of the transmitted THz pulses were obtained as the difference or the sum of the transmitted THz pulses with the polarizers set as 45° and −45°. The rotation

© 2022 The Author(s). Published by the Royal Society of Chemistry

Open Access Article. Published on 23 September 2022. Downloaded on 2/28/2025 12:12:53 PM.
This article is licensed under a Creative Commons Attribution-NonCommercial 3.0 Unported Licence.

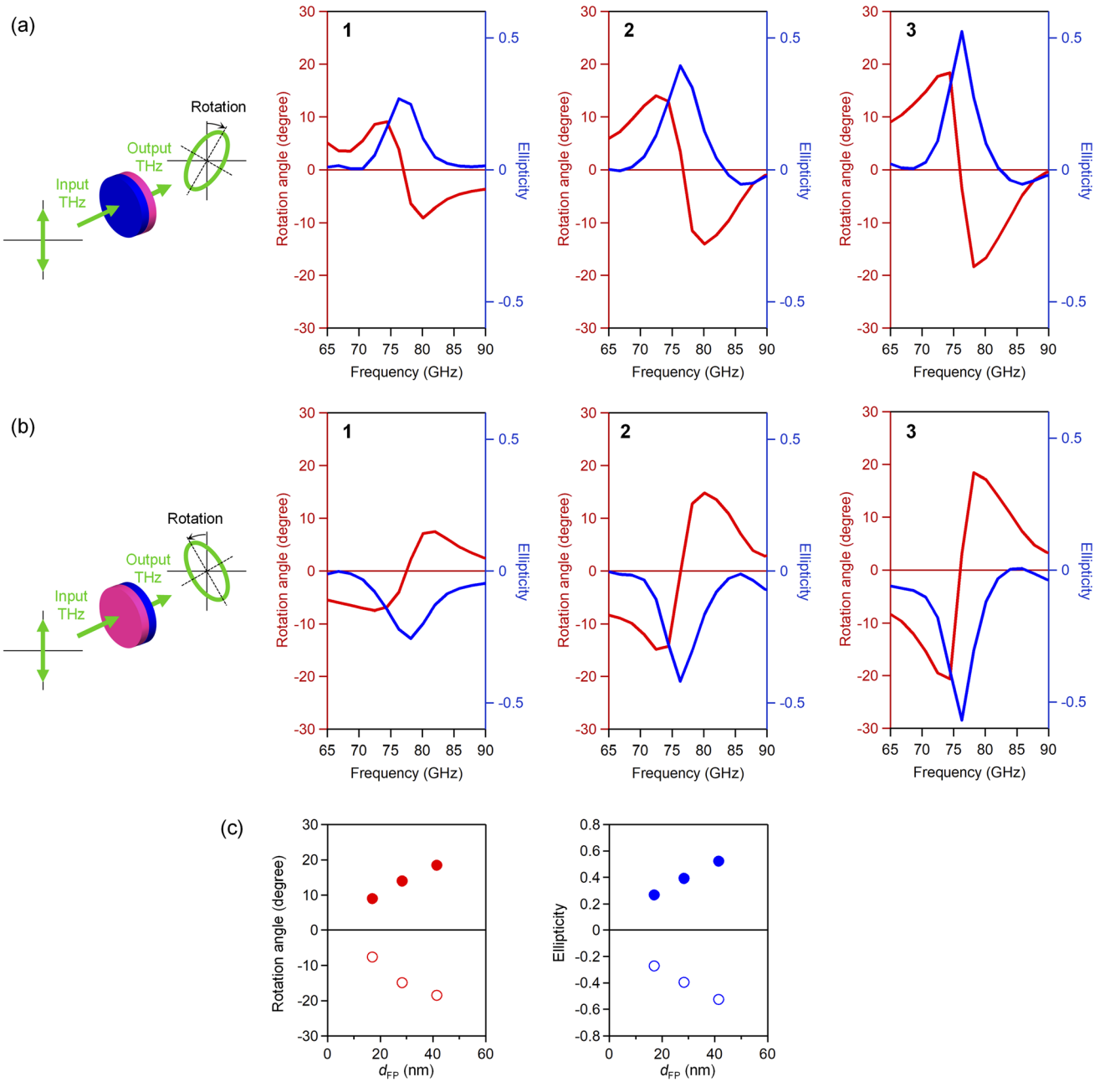

Fig. 3 (a) and (b) Faraday rotation angle (red) and Faraday ellipticity (blue) measured by THz-TDS. The incident THz pulse was irradiated from S-pole (a) and N-pole (b) of the magnetized pellet sample. Left figures show the schematic illustration of the millimeter wave rotation. (c) Faraday rotation angle and Faraday ellipticity *versus* the particle size, measured by irradiating THz pulse from the S-pole side (close circles) and the N-pole side (open circles) of the magnetized pellets.

angle and ellipticity of the transmitted light were obtained from the vertical and horizontal components. Prior to the measurements, the pellet samples were magnetized by placing the pellet under a magnetic field of 8 tesla.

Fig. 3a shows the rotation angle and ellipticity in the millimeter-wave region, where the incident THz pulse was irradiated from the S-pole of the magnetized pellet sample. The rotation angle spectrum shows the dispersive shape centered at the peak frequency of ellipticity. The rotation angle increases as the particle size becomes larger: 9.1° (**1**), 14.1° (**2**), and 18.4° (**3**). The Faraday ellipticity shows the peak at the same frequency as the absorption peak frequency. The ellipticity increases with increasing the particle size: 0.27 (**1**), 0.39 (**2**), and 0.52 (**3**). Irradiating the incident THz pulse from the opposite pole, N-pole, the signs of rotation angle and ellipticity change (Fig. 3b and c).

Mechanism of particle size effect

Here, we consider the particle size effect on millimeter-wave absorption. The plot of the absorption *versus* the particle size

Open Access Article. Published on 23 September 2022. Downloaded on 2/28/2025 12:12:53 PM.
This article is licensed under a Creative Commons Attribution-NonCommercial 3.0 Unported Licence.

shows that the absorption decreases as the particle size decreases (Fig. 4). We assume that this decrease is due to the loss of ferromagnetism of the iron atoms near the surface. The TEM images show that the present materials are composed of nanoparticles. The volume of the core and the total volume of the particle are expressed as $4\pi(d/2 - d_s)^3/3$ and $4\pi(d/2)^3/3$, respectively, where d_s shows the thickness from the surface.

Therefore, the ratio of the core volume to the total particle volume is $\{4\pi(d/2 - d_s)^3/3\}/\{4\pi(d/2)^3/3\}$. Assuming that the core contributes to absorption, the absorption area (A) is described by

$$A = A_\infty\{4\pi(d/2 - d_s)^3/3\}/\{4\pi(d/2)^3/3\}, \quad (1)$$

where A_∞ is the absorption area without the surface effects. The particle size dependence of the absorption is well fitted by eqn (1), indicating that the ferromagnetism near the surface layer is lost. Hence, millimeter-waves cannot be absorbed at the surface. The fitted value of $d_s = 1.6$ nm almost corresponds to one unit cell of the crystal structure. The value of $A_\infty = 73$ dB GHz is the intrinsic absorption of the present series with a filling ratio of 60 vol%, which corresponds to 120 dB GHz mm^{-1}. Therefore, a larger particle size may realize a larger absorption as a millimeter-wave absorber and a larger Faraday rotation and ellipticity effect in the millimeter-wave region.

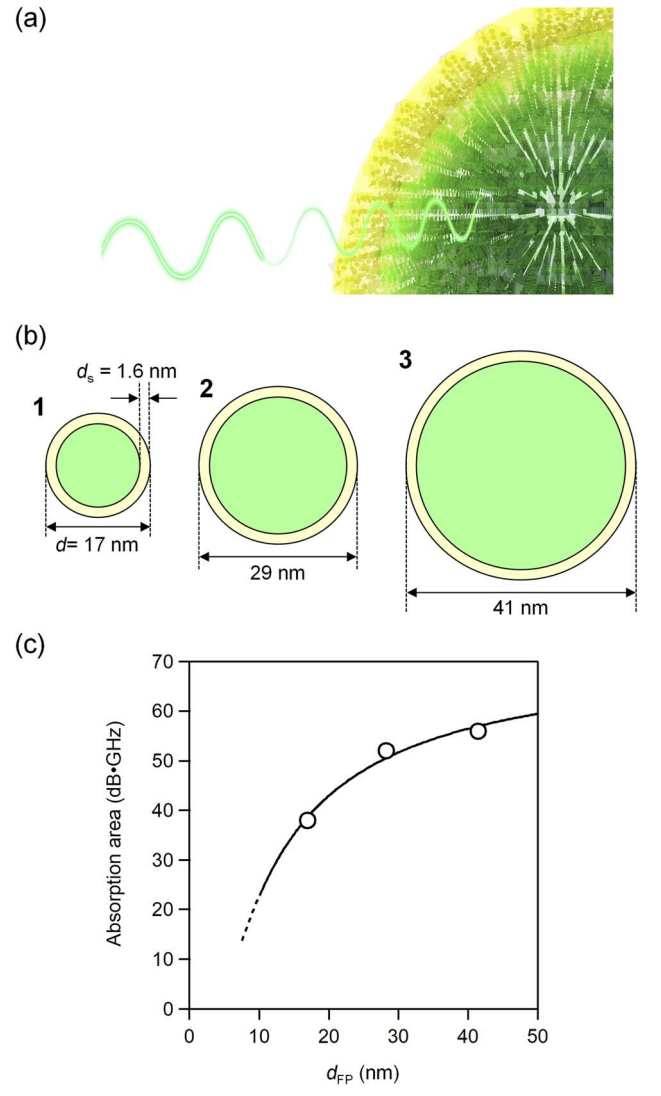

Fig. 4 (a) Schematic illustration of millimeter wave absorption. The core (green) absorbs millimeter waves but the surface (yellow) does not. (b) Schematic illustration of the nanoparticles of **1–3** showing the thickness from the surface d_s. (c) Absorption peak area *versus* the particle size (open circles) and the fitted line by eqn (1) (solid line).

Conclusions

Herein the millimeter-wave absorption, rotation, and ellipticity of ε-$Ga_xFe_{2-x}O_3$ with various particle sizes were investigated. Increasing the particle size improves the millimeter-wave absorption and rotation properties of ε-$Ga_xFe_{2-x}O_3$. Analysis of the particle size dependence indicates that ferromagnetism near the surface layer is lost, inhibiting the absorption of millimeter-waves. The thickness of 1.6 nm almost corresponds to one unit cell of the crystal structure. Therefore, a larger particle size may achieve a larger absorption for an absorber as well as a larger Faraday rotation and ellipticity effect in the millimeter-wave region.

Conflicts of interest

There are no conflicts to declare.

Acknowledgements

This work was supported in part by a Grant-in-Aid for Scientific Research (A) from the Japan Society for the Promotion of Science (JSPS) (Grant Number 20H00369). S. S. acknowledges the support of Materials Education program for the Future Leaders in Research, Industry, and Technology (MERIT). We recognize the Cryogenic Research Center at The University of Tokyo, DOWA Technofund, and the Center for Nano Lithography & Analysis at The University of Tokyo.

Notes and references

1 J. Hasch, E. Topak, R. Schnabel, T. Zwick, R. Weigel and C. Waldschmidt, *IEEE Trans. Microwave Theory Tech.*, 2012, **60**, 845–860.
2 S. Patole, M. Torlak, D. Wang and M. Ali, *IEEE Signal Processing Magazine*, 2017, **34**, 22–35.
3 K. Yoneda, N. Suganuma, R. Yanase and M. Aldibaja, *IATSS Research*, 2019, **43**, 253–262.
4 D. Barnes, M. Gadd, P. Murcutt, P. Newman and I. Posner, *Proceedings of IEEE International Conference on Robotics and Automation*, 2020, 6433–6438.
5 S. Geetha, K. K. Satheesh Kumar, C. R. K. Rao, M. Vijayan and D. C. Trivedi, *J. Appl. Polym. Sci.*, 2009, **112**, 2073–2086.
6 C. M. Watts, X. Liu and W. J. Padilla, *Adv. Mater.*, 2012, **24**, OP98–OP120.
7 M. Pardavi-Horvath, *J. Magn. Magn. Mater.*, 2000, **215–216**, 171–183.

© 2022 The Author(s). Published by the Royal Society of Chemistry

Open Access Article. Published on 23 September 2022. Downloaded on 2/28/2025 12:12:53 PM.
This article is licensed under a Creative Commons Attribution-NonCommercial 3.0 Unported Licence.

8 J. D. Adam, L. E. Davis, G. F. Dionne, E. F. Schloemann and S. N. Stitzer, *IEEE Trans. Microwave Theory Tech.*, 2002, **50**, 721–737.
9 R. K. Selvan, V. Krishnan, C. O. Augustin, H. Bertagnolli, C. S. Kim and A. Gedanken, *Chem. Mater.*, 2008, **20**, 429–439.
10 V. G. Harris, *IEEE Trans. Magn.*, 2012, **48**, 1075–1104.
11 X. Huang, J. Zhang, M. Lai and T. Sang, *J. Alloys Compd.*, 2015, **627**, 367–373.
12 X. Yang, Z. Zhou, T. Nan, Y. Gao, G. M. Yang, M. Liu and N. X. Sun, *J. Mater. Chem. C*, 2016, **4**, 234–243.
13 A. Houbi, Z. A. Aldashevich, Y. Atassi, Z. B. Telmanovna, M. Saule and K. Kubanych, *J. Magn. Magn. Mater.*, 2021, **529**, 167839.
14 D. Liu, Y. Du, P. Xu, N. Liu, Y. Wang, H. Zhao, L. Cui and X. Han, *J. Mater. Chem. C*, 2019, **7**, 5037–5046.
15 J. Shen, Y. Yao, Y. Liu and J. Leng, *J. Mater. Chem. C*, 2016, **4**, 7614–7621.
16 B. D. Cullity and C. D. Graham, *Introduction to Magnetic Materials*, Wiley-IEEE Press, New Jersey, 2nd edn, 2008.
17 A. Goldman, *Modern Ferrite Technology*, Springer, New York, 2nd edn, 2006.
18 J. Jin, S. Ohkoshi and K. Hashimoto, *Adv. Mater.*, 2004, **16**, 48–51.
19 E. Tronc, C. Chanéac, J. P. Jolivet and J. M. Grenèche, *J. Appl. Phys.*, 2005, **98**, 053901.
20 J. Jin, K. Hashimoto and S. Ohkoshi, *J. Mater. Chem.*, 2005, **15**, 1067–1071.
21 S. Sakurai, J. Jin, K. Hashimoto and S. Ohkoshi, *J. Phys. Soc. Jpn.*, 2005, **74**, 1946–1949.
22 Y.-C. Tseng, N. M. Souza-Neto, D. Haskel, M. Gich, C. Frontera, A. Roig, M. van Veenendaal and J. Nogués, *Phys. Rev. B: Condens. Matter Mater. Phys.*, 2009, **79**, 094404.
23 J. Tuček, R. Zbořil, A. Namai and S. Ohkoshi, *Chem. Mater.*, 2010, **22**, 6483–6505.
24 M. Gich, I. Fina, A. Morelli, F. Sánchez, M. Alexe, J. Gàzquez, J. Fontcuberta and A. Roig, *Adv. Mater.*, 2014, **26**, 4645–4652.
25 G. Carraro, A. Gasparotto, C. Maccato, V. Gombac, F. Rossi, T. Montini, D. Peeters, E. Bontempi, C. Sada, D. Barreca and P. Fornasiero, *RSC Adv.*, 2014, **4**, 32174–32179.
26 S. Bhattacharya, A. Roychowdhury, D. Das and S. Nayar, *RSC Adv.*, 2015, **5**, 89488–89497.
27 S. Ohkoshi, A. Namai, K. Imoto, M. Yoshikiyo, W. Tarora, K. Nakagawa, M. Komine, Y. Miyamoto, T. Nasu, S. Oka and H. Tokoro, *Sci. Rep.*, 2015, **5**, 14414.
28 J. López-Sánchez, A. Muñoz-Noval, A. Serrano, M. Abuín, J. de la Figuera, J. F. Marco, L. Pérez, N. Carmona and O. Rodríguez de la Fuente, *RSC Adv.*, 2016, **6**, 46380–46387.
29 S. Ohkoshi, A. Namai, T. Yamaoka, M. Yoshikiyo, K. Imoto, T. Nasu, S. Anan, Y. Umeta, K. Nakagawa and H. Tokoro, *Sci. Rep.*, 2016, **6**, 27212.
30 J. L. García-Muñoz, A. Romaguera, F. Fauth, J. Nogués and M. Gich, *Chem. Mater.*, 2017, **29**, 9705–9713.
31 K. T. Chan, J. R. Morales, Y. Kodera and J. E. Garay, *J. Mater. Chem. C*, 2017, **5**, 7911–7918.
32 V. Ukleev, S. Suturin, T. Nakajima, T. Arima, T. Saerbeck, T. Hanashima, A. Sitnikova, D. Kirilenko, N. Yakovlev and N. Sokolov, *Sci. Rep.*, 2018, **8**, 8741.
33 J. A. Sans, V. Monteseguro, G. Garbarino, M. Gich, V. Cerantola, V. Cuartero, M. Monte, T. Irifune, A. Muñoz and C. Popescu, *Nat. Commun.*, 2018, **9**, 4554.
34 S. Ohkoshi, K. Imoto, A. Namai, M. Yoshikiyo, S. Miyashita, H. Qiu, S. Kimoto, K. Kato and M. Nakajima, *J. Am. Chem. Soc.*, 2019, **141**, 1775–1780.
35 J. Yuan, A. Balk, H. Guo, Q. Fang, S. Patel, X. Zhao, T. Terlier, D. Natelson, S. Crooker and J. Lou, *Nano Lett.*, 2019, **19**, 3777–3781.
36 J. López-Sánchez, A. Serrano, A. del Campo, M. Abuín, E. Salas-Colera, A. Muñoz-Noval, G. R. Castro, J. de la Figuera, J. F. Marco, P. Marín, N. Carmona and O. Rodríguez de la Fuente, *RSC Adv.*, 2019, **9**, 17571–17580.
37 J. Ma, Y. Wang and K. Chen, *Adv. Powder Technol.*, 2019, **30**, 3021–3027.
38 H. Tokoro, J. Fukui, K. Watanabe, M. Yoshikiyo, A. Namai and S. Ohkoshi, *RSC Adv.*, 2020, **10**, 39611–39616.
39 Y. Gu, M. Yoshikiyo, A. Namai, D. Bonvin, A. Martinez, R. Piñol, P. Téllez, N. J. O. Silva, F. Ahrentorp, C. Johansson, J. Marco-Brualla, R. Moreno-Loshuertos, P. Fernández-Silva, Y. Cui, S. Ohkoshi and A. Millán, *RSC Adv.*, 2020, **10**, 28786–28797.
40 S. Ohkoshi, M. Yoshikiyo, K. Imoto, K. Nakagawa, A. Namai, H. Tokoro, Y. Yahagi, K. Takeuchi, F. Jia, S. Miyashita, M. Nakajima, H. Qiu, K. Kato, T. Yamaoka, M. Shirata, K. Naoi, K. Yagishita and H. Doshita, *Adv. Mater.*, 2020, **32**, 2004897.
41 Y. Kusano, H. Nakata, Z. Peng, R. S. S. Maki, T. Ogawa and M. Fukuhara, *ACS Appl. Mater. Interfaces*, 2021, **13**, 38491–38498.
42 Y. Gu, N. J. O. Silva, M. Yoshikiyo, A. Namai, R. Piñol, G. Maurin-Pasturel, Y. Cui, S. Ohkoshi, A. Millán and A. Martínez, *Chem. Commun.*, 2021, **57**, 2285–2288.
43 A. Philip, Y. Zhou, G. C. Tewari, S. van Dijken and M. Karppinen, *J. Mater. Chem. C*, 2022, **10**, 294–300.
44 H. Tokoro, K. Nakabayashi, S. Nagashima, Q. Song, M. Yoshikiyo and S. Ohkoshi, *Bull. Chem. Soc. Jpn.*, 2022, **95**, 538–552.
45 E. Gorbachev, M. Soshnikov, M. Wu, L. Alyabyeva, D. Myakishev, E. Kozlyakova, V. Lebedev, E. Anokhin, B. Gorshunov, O. Brylev, P. Kazin and L. Trusov, *J. Mater. Chem. C*, 2021, **9**, 6173–6179.
46 A. Namai, S. Sakurai, M. Nakajima, T. Suemoto, K. Matsumoto, M. Goto, S. Sasaki and S. Ohkoshi, *J. Am. Chem. Soc.*, 2009, **131**, 1170–1173.
47 A. Namai, M. Yoshikiyo and S. Ohkoshi, *IEEE Magn. Lett.*, 2016, **7**, 5506704.
48 Y. Hamasaki, T. Shimizu, S. Yasui, T. Shiraishi, A. Akama, T. Kiguchi, T. Taniyama and M. Itoh, *J. Appl. Phys.*, 2017, **122**, 015301.
49 L. Corbellini, C. Lacroix, D. Ménard and A. Pignolet, *Scr. Mater.*, 2017, **140**, 63–66.
50 K. Knížek, M. Pashchenko, P. Levinský, O. Kaman, J. Houdková, P. Jiříček, J. Hejtmánek, M. Soroka and J. Buršík, *J. Appl. Phys.*, 2018, **124**, 213904.

Open Access Article. Published on 23 September 2022. Downloaded on 2/28/2025 12:12:53 PM.
This article is licensed under a Creative Commons Attribution-NonCommercial 3.0 Unported Licence.

51 L. Kubíčková, O. Kaman, P. Veverka, V. Herynek, P. Brázda, M. Vosmanská, T. Kmječ, P. Dvořák, D. Kubániová and J. Kohout, *Colloids Surf., A*, 2020, **589**, 124423.
52 S. Ohkoshi, S. Kuroki, S. Sakurai, K. Matsumoto, K. Sato and S. Sasaki, *Angew. Chem., Int. Ed.*, 2007, **46**, 8392–8395.
53 M. Nakajima, A. Namai, S. Ohkoshi and T. Suemoto, *Opt. Express*, 2010, **18**, 18260–18268.
54 T. Katayama, S. Yasui, Y. Hamasaki and M. Itoh, *Appl. Phys. Lett.*, 2017, **110**, 212905.
55 L. Kubíčková, O. Kaman, P. Veverka, V. Herynek, P. Brázda, K. Bernášek, M. Veverka and J. Kohout, *J. Alloys Compd.*, 2021, **856**, 158187.
56 S. Sakurai, S. Kuroki, H. Tokoro, K. Hashimoto and S. Ohkoshi, *Adv. Funct. Mater.*, 2007, **17**, 2278–2282.
57 M. Yoshikiyo, A. Namai, M. Nakajima, K. Yamaguchi, T. Suemoto and S. Ohkoshi, *J. Appl. Phys.*, 2014, **115**, 172613.
58 A. Namai, M. Yoshikiyo, K. Yamada, S. Sakurai, T. Goto, T. Yoshida, T. Miyazaki, M. Nakajima, T. Suemoto, H. Tokoro and S. Ohkoshi, *Nat. Commun.*, 2012, **3**, 1035.
59 A. Namai, M. Yoshikiyo, S. Umeda, T. Yoshida, T. Miyazaki, M. Nakajima, K. Yamaguchi, T. Suemoto and S. Ohkoshi, *J. Mater. Chem. C*, 2013, **1**, 5200–5206.
60 S. Ohkoshi, K. Imoto, A. Namai, S. Anan, M. Yoshikiyo and H. Tokoro, *J. Am. Chem. Soc.*, 2017, **139**, 13268–13271.
61 S. Yasui, T. Katayama, T. Osakabe, Y. Hamasaki, T. Taniyama and M. Itoh, *J. Ceram. Soc. Jpn.*, 2019, **127**, 474–477.
62 S. Tsukamoto, Y. Oki, K. Imoto, A. Namai, M. Yoshikiyo and S. Ohkoshi, *Advanced Photonics Research*, 2022, **3**, 2100319.
63 P. Goyal and N. K. Prasad, *IEEE Trans. Magn.*, 2016, **52**, 2300906.
64 I. Ahamed, R. Skomski and A. Kashyap, *AIP Adv.*, 2019, **9**, 035231.
65 Z. Ma, A. Romaguera, F. Fauth, J. Herrero-Martín, J. L. García-Muñoz and M. Gich, *J. Magn. Magn. Mater.*, 2020, **506**, 166764.
66 M. Polášková, O. Malina, J. Tuček and P. Jakubec, *Nanoscale*, 2022, **14**, 5501–5513.
67 T. Katayama, S. Yasui, Y. Hamasaki, T. Osakabe and M. Itoh, *J. Mater. Chem. C*, 2017, **5**, 12597–12601.
68 A. Namai, K. Ogata, M. Yoshikiyo and S. Ohkoshi, *Bull. Chem. Soc. Jpn.*, 2020, **93**, 20–25.
69 R. Kinugawa, K. Imoto, Y. Futakawa, S. Shimizu, R. Fujiwara, M. Yoshikiyo, A. Namai and S. Ohkoshi, *Adv. Eng. Mater.*, 2021, **23**, 2001473.
70 M. Yoshikiyo, Y. Futakawa, R. Shimoharai, Y. Ikeda, J. MacDougall, A. Namai and S. Ohkoshi, *Chem. Phys. Lett.*, 2022, **803**, 139821.
71 M. Gich, C. Frontera, A. Roig, E. Taboada, E. Molins, H. R. Rechenberg, J. D. Ardisson, W. A. A. Macedo, C. Ritter, V. Hardy, J. Sort, V. Skumryev and J. Nogués, *Chem. Mater.*, 2006, **18**, 3889–3897.
72 S. Ohkoshi, A. Namai and S. Sakurai, *J. Phys. Chem. C*, 2009, **113**, 11235–11238.
73 J. Tucek, S. Ohkoshi and R. Zboril, *Appl. Phys. Lett.*, 2011, **99**, 253108.
74 M. Yoshikiyo, K. Yamada, A. Namai and S. Ohkoshi, *J. Phys. Chem. C*, 2012, **116**, 8688–8691.
75 I. Ahamed, N. Seriani, R. Gebauer and A. Kashyap, *RSC Adv.*, 2020, **10**, 27474–27480.
76 Y. V. Knyazev, A. I. Chumakov, A. A. Dubrovskiy, S. V. Semenov, I. Sergueev, S. S. Yakushkin, V. L. Kirillov, O. N. Martyanov and D. A. Balaev, *Phys. Rev. B*, 2020, **101**, 094408.

© 2022 The Author(s). Published by the Royal Society of Chemistry